Supplementary Information

Air-Stable Lithium-Sandwiched Current Collector for Non-Destructive, Thermally safe, and Sustained Supplementary Lithiation

Can Zhang†, Xinlong Chen†, Wang Wan, Ganxiong Liu, Quan Nie, Fangzhou Yang, Xueyang Li, Sa Li, Yunhui Huang and Chao Wang*

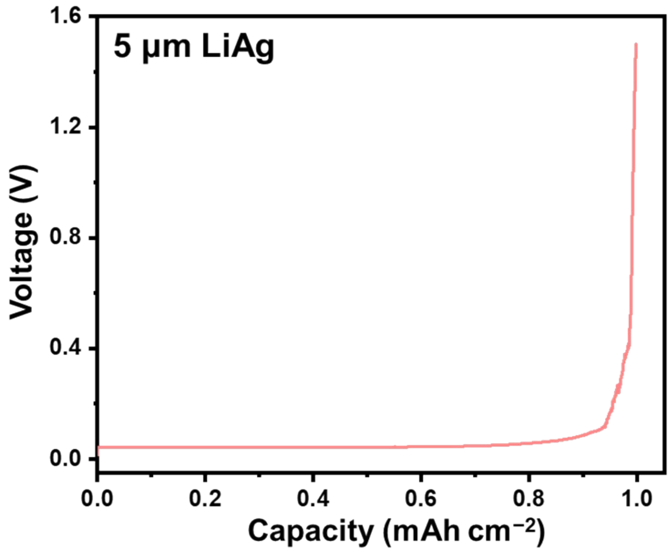

Figure S1. The delithiation curve of 5 μm-thick LiAg alloy foil.

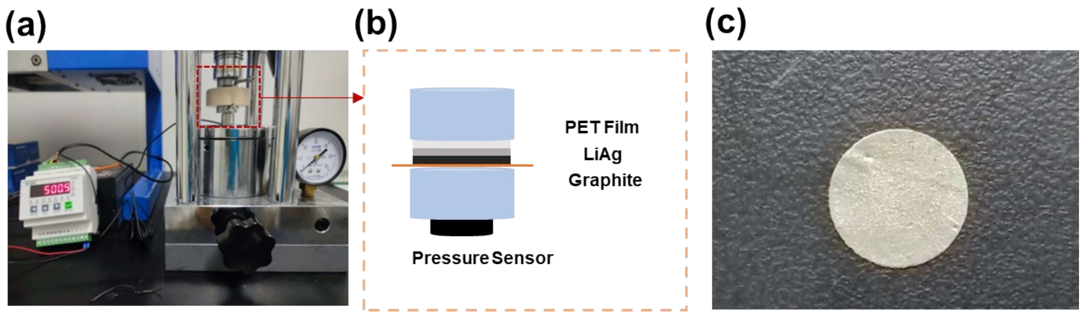

Figure S2. (a-b) The illustration of device for applying pressure for contact prelithiation. (c) The photograph of Gr/LiAg electrode before applying pressure.

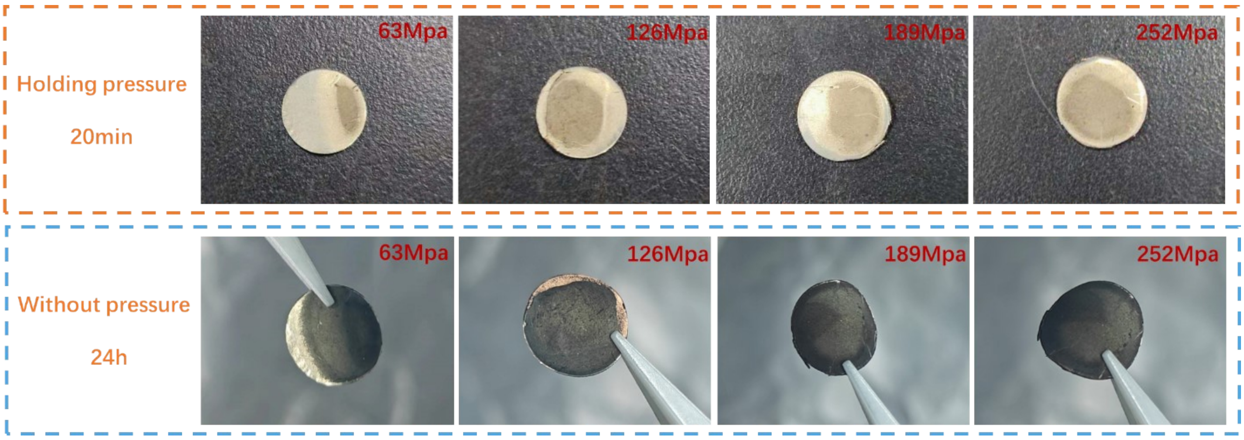

Figure S3. The color changes of Gr/LiAg electrode after applying different pressure and duration.

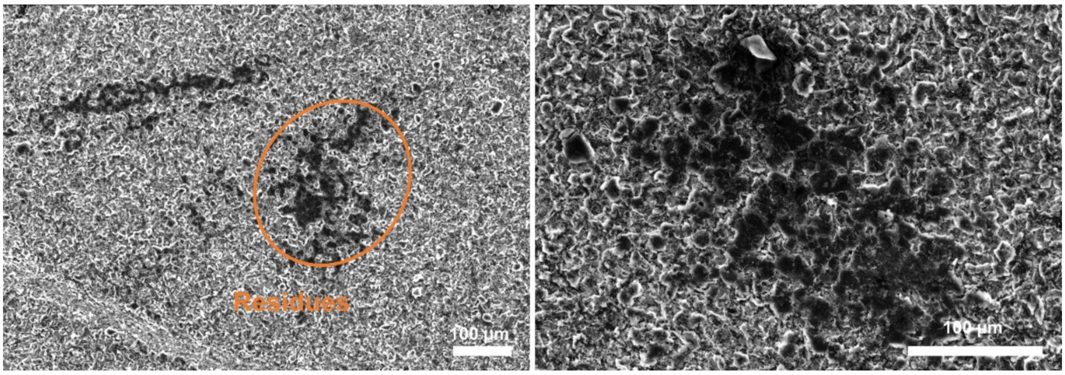

Figure S4. The SEM images of Gr/LiAg electrode after 24-h rest in the glove box.

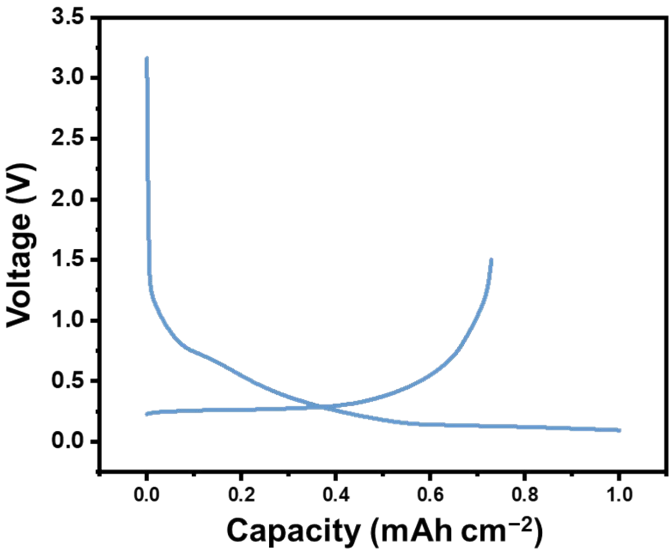

Figure S5. The voltage-capacity curve of the electrochemical prelithiation of 1 mAh cm^{-2}.

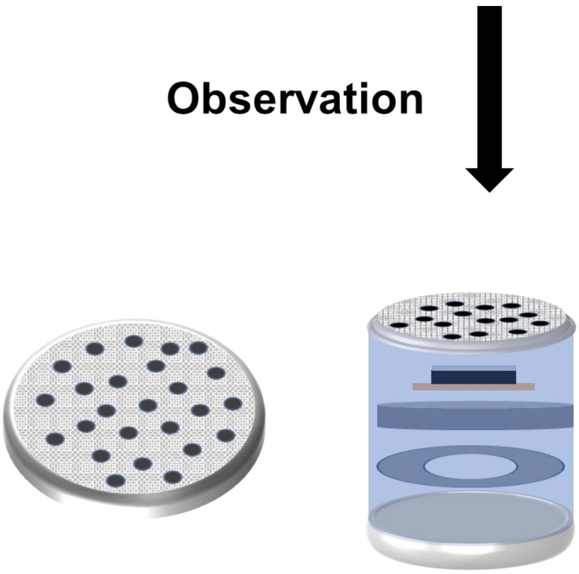

Figure S6. In-situ observation of contact prelithiation process.

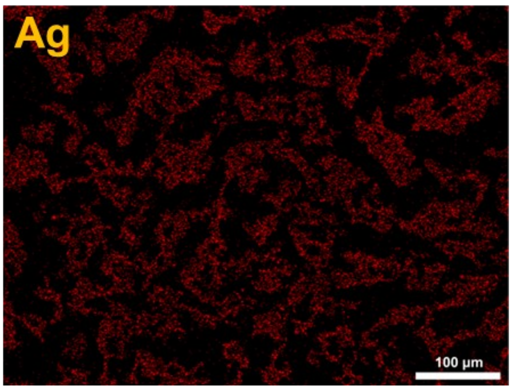

Figure S7. The distribution of element Ag within surficial alloy residues.

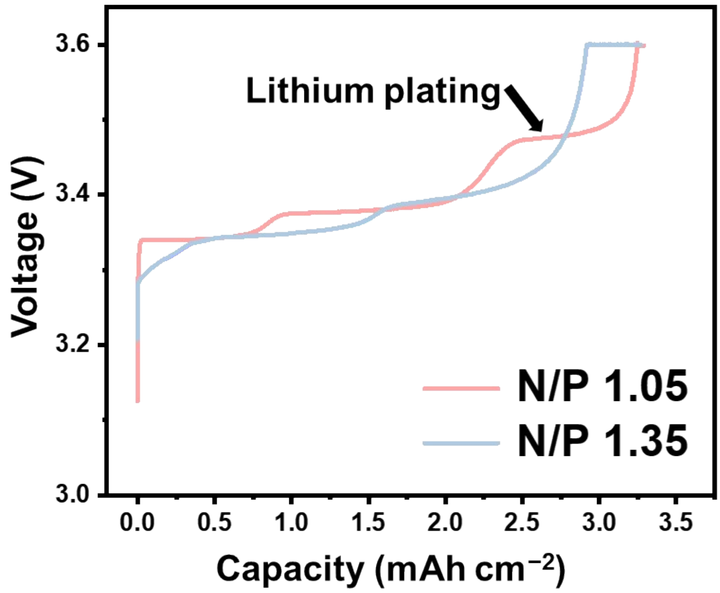

Figure S8. The charging curve of LFP||Gr-Contact prelithiation full cells with different N/P ratios.

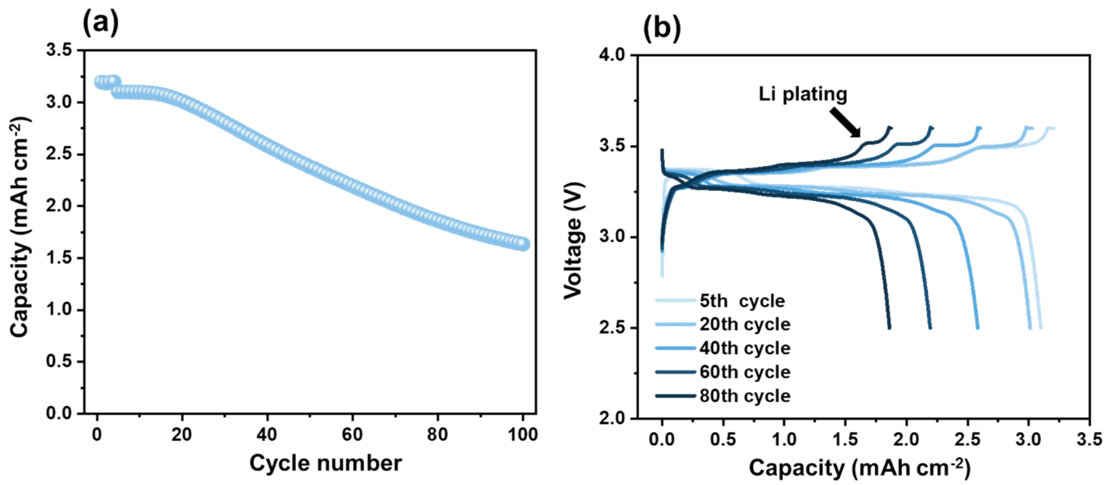

Figure S9. (a) The cycling performance and (b) the charge-discharge curves of the LFP||Gr contact prelithiation cell with an N/P ratio of 1.05.

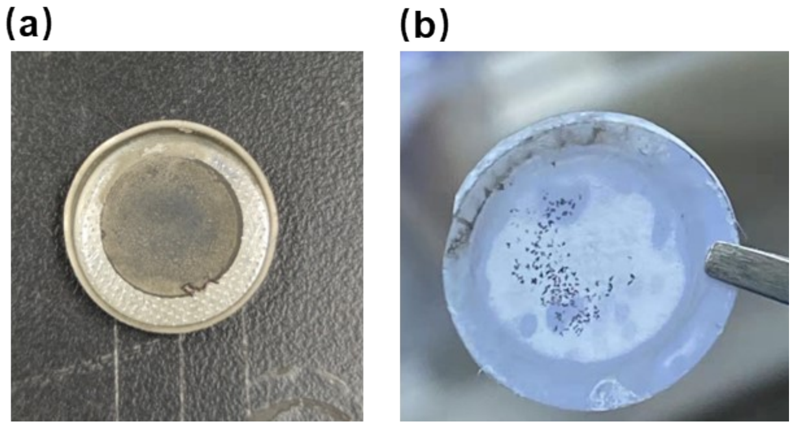

Figure S10. The residues on anode (a) and separator (b).

Figure S11. The photo of Cu-Li-Cu with extruded lithium.

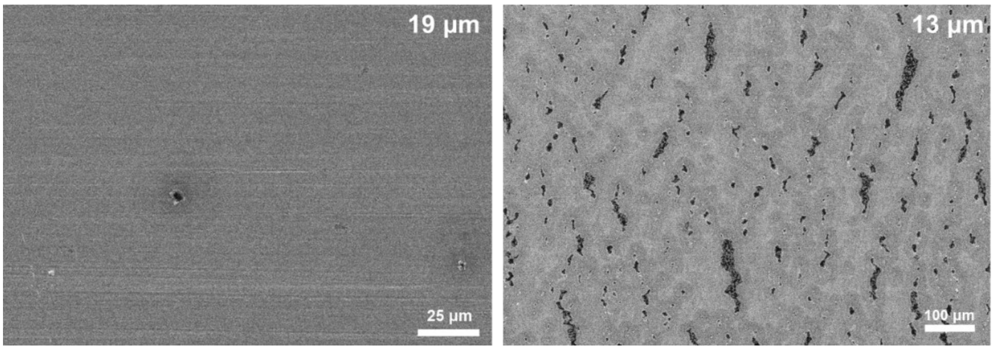

Figure S12. The morphology of the surface hole on CLC of 19 μm and 13 μm thick.

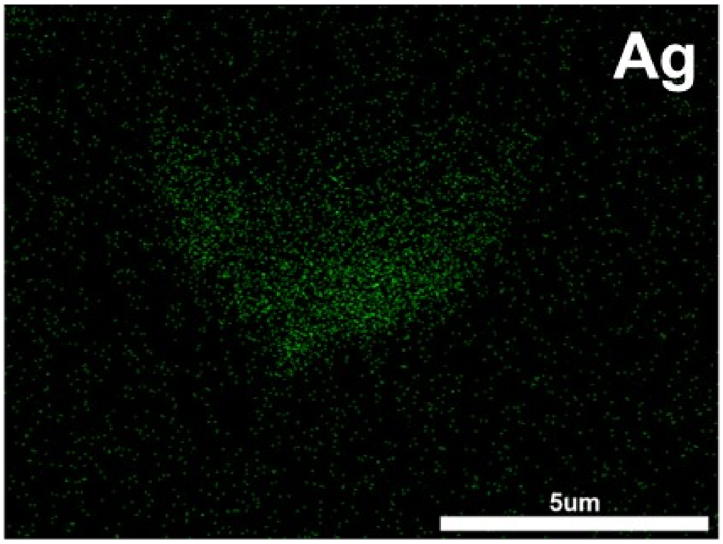

Figure S13. The distribution of element Ag within holes of CLC-16.

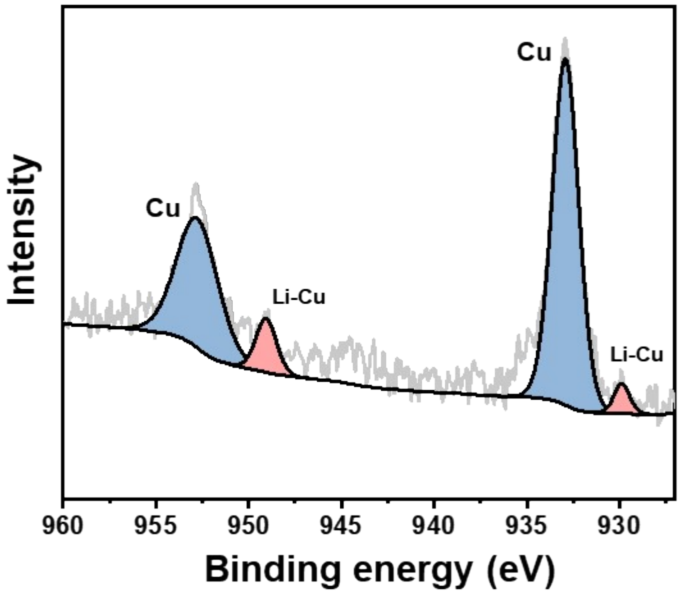

Figure S14. The XPS result of Cu element at LiAg/Cu interface.

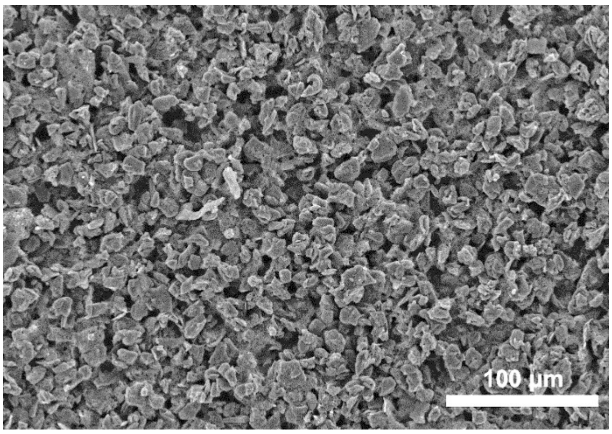

Figure S15. The surface morphology of graphite electrode on Cu foil.

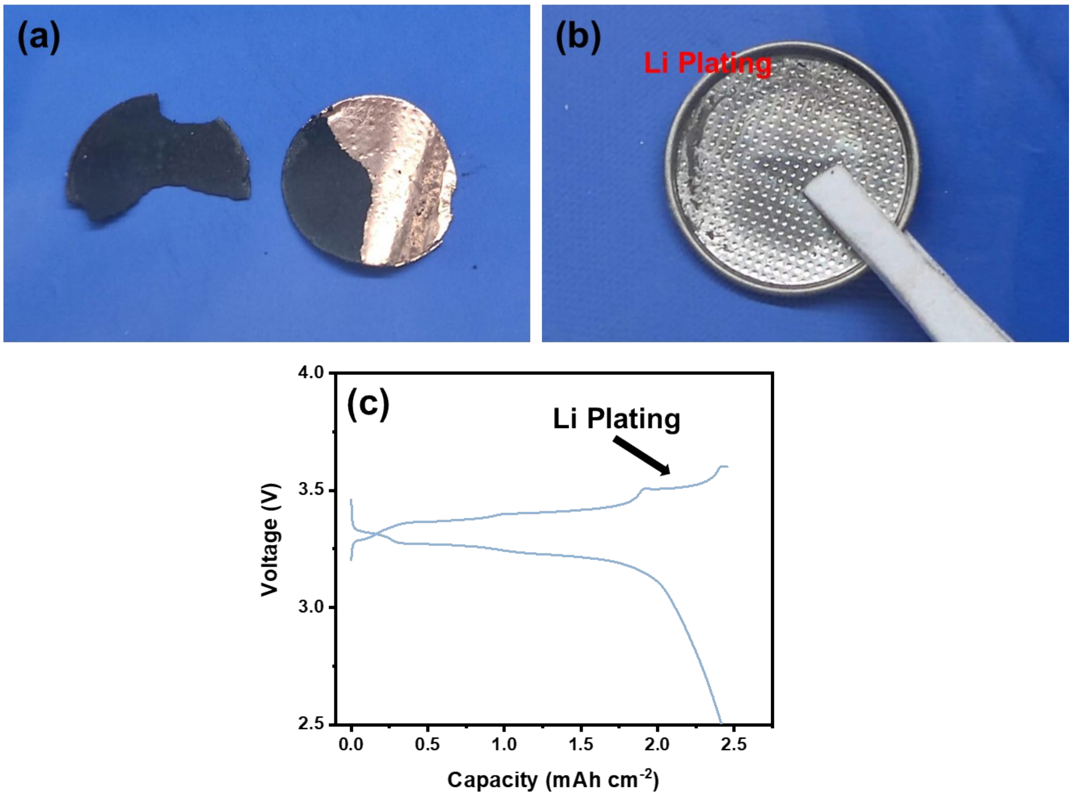

Figure S16. (a) Delamination of bulk graphite from CLC-13. (b) Lithium deposition surrounding the graphite electrode. (c) Voltage-Capacity curve of the 95th cycle for LFP||Gr-CLC-13 full cell.

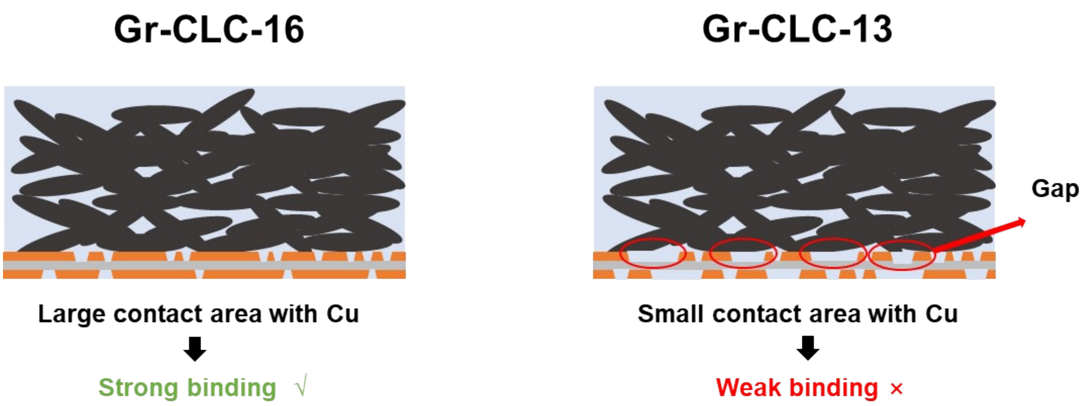

Figure S17. The decreased contact area between CLC-13 and active material after lithium dissolution.

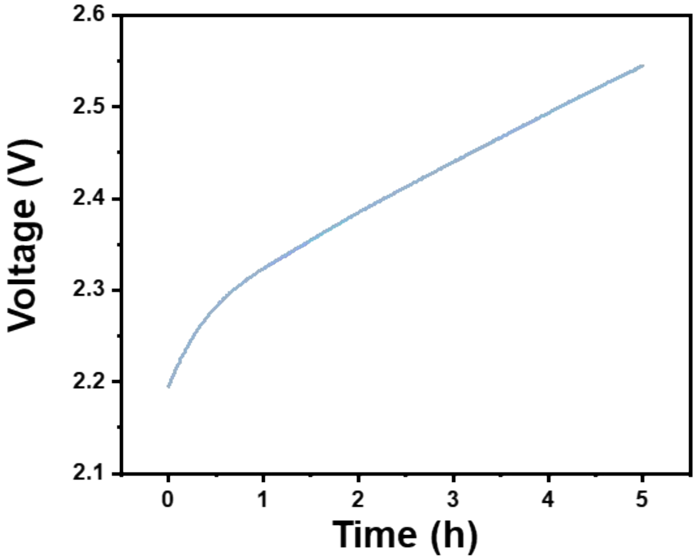

Figure S18. The voltage change of LFP||Gr-CLC-16 full cell during rest procedure.

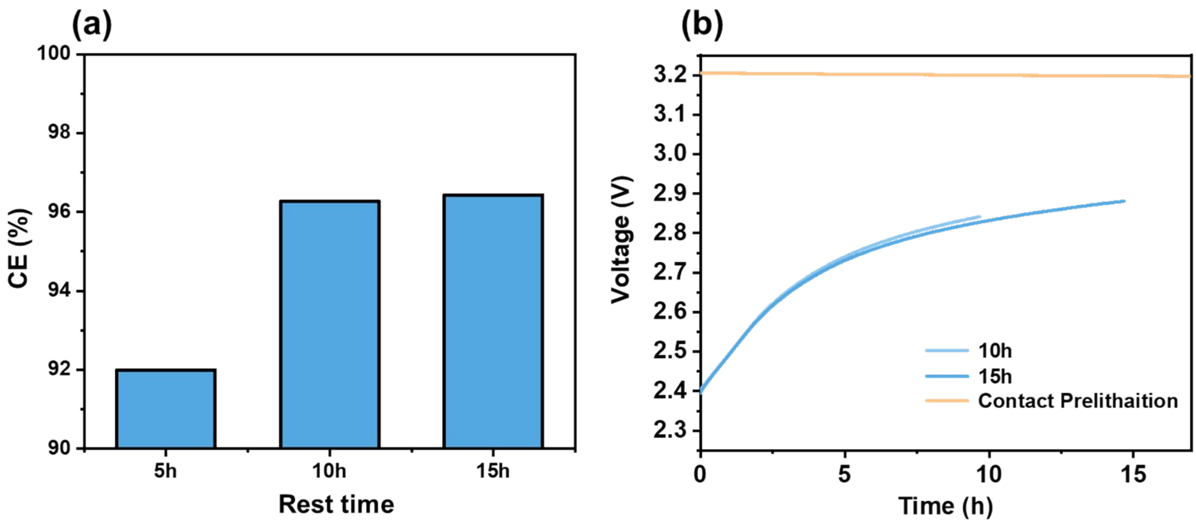

Figure S19. (a) The ICE change of LFP||Gr-CLC-16 after different rest times. (b) The voltage changes of LFP||Gr-CLC-16 during the rest period.

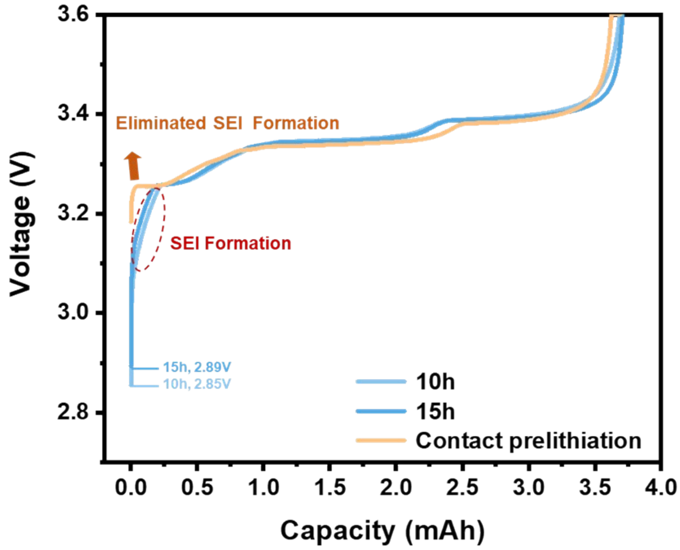

Figure S20. The initial charging curve of the LFP||Gr-CLC-16 cell after different rest times. The LFP||Gr-Contact prelithiation was used as a comparison.

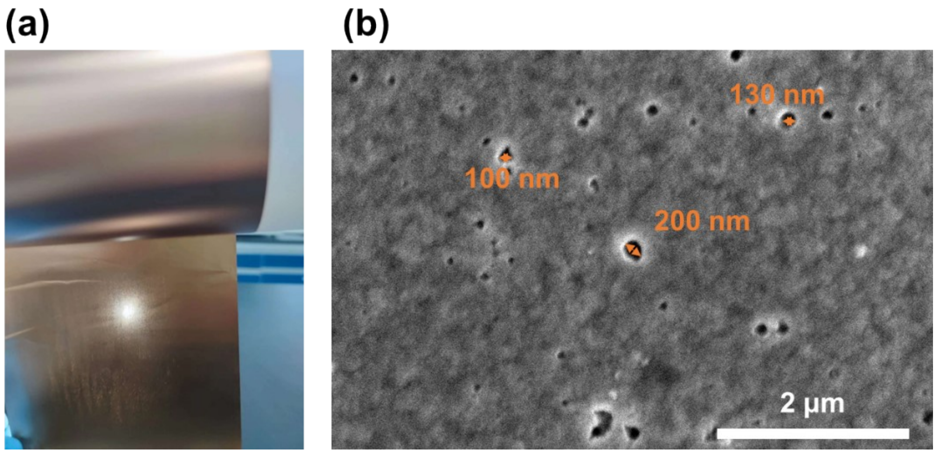

Figure S21. The porous Cu foil with pore sizes lower than 200nm.

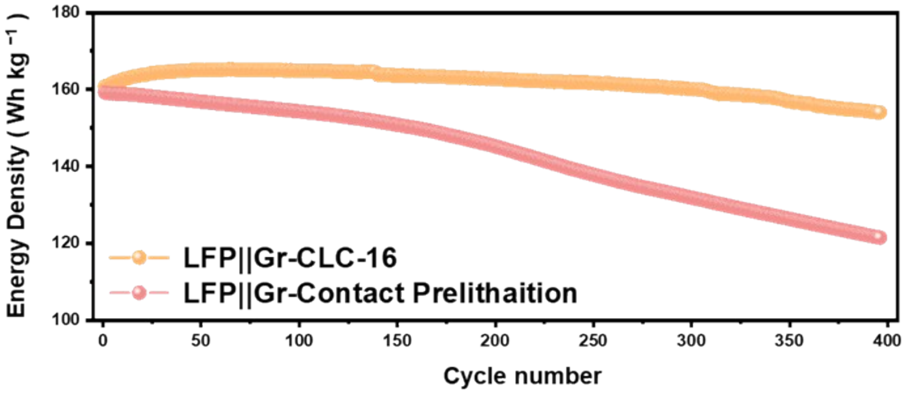

Figure S22. The energy density comparison between LFP||Gr-CLC-16 and LFP||Gr-Contact prelithiation.

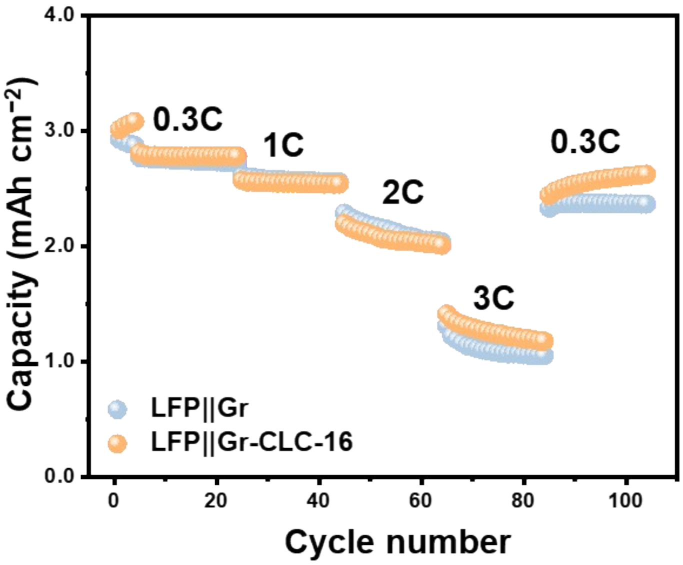

Figure S23. The rate performance of LFP||Gr-CLC-16 full cell.

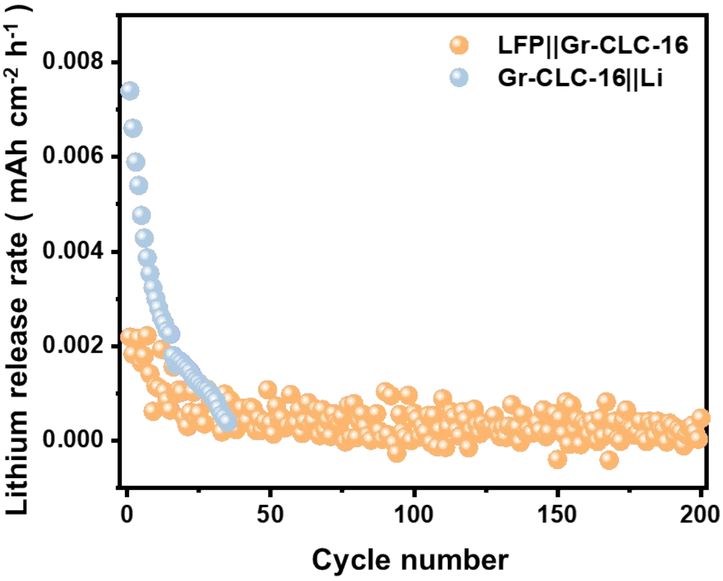

Figure S24. The lithium release rate comparison for LFP||Gr-CLC-16 and Gr-CLC-16||Li.

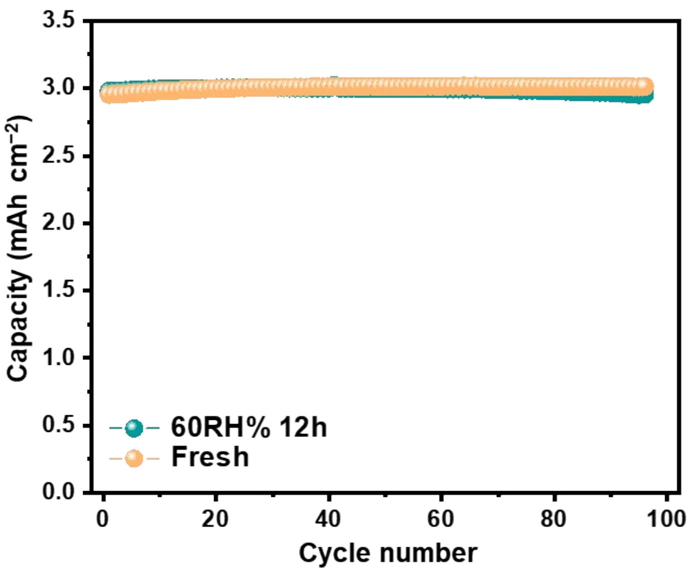

Figure S25. The cycling performance of LFP||Gr-CLC-16 full cell after being exposed to air for 12h.

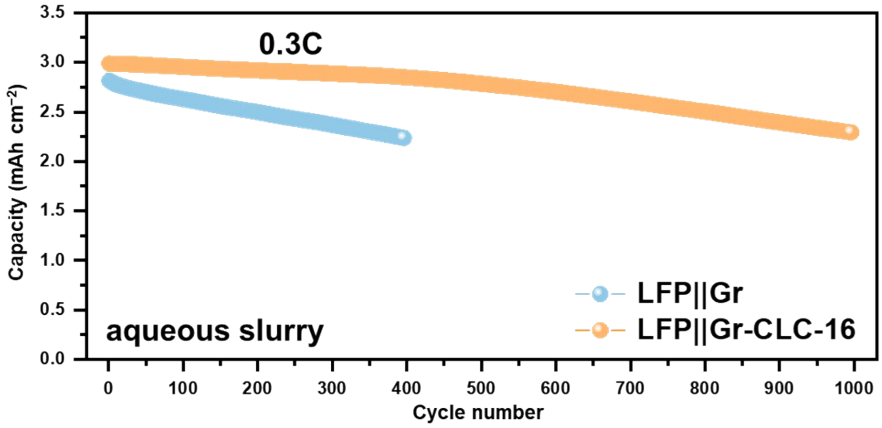

Figure S26. The long-term cycling performance of LFP||Gr-CLC-16 full cell using water as coating slurry solvent.

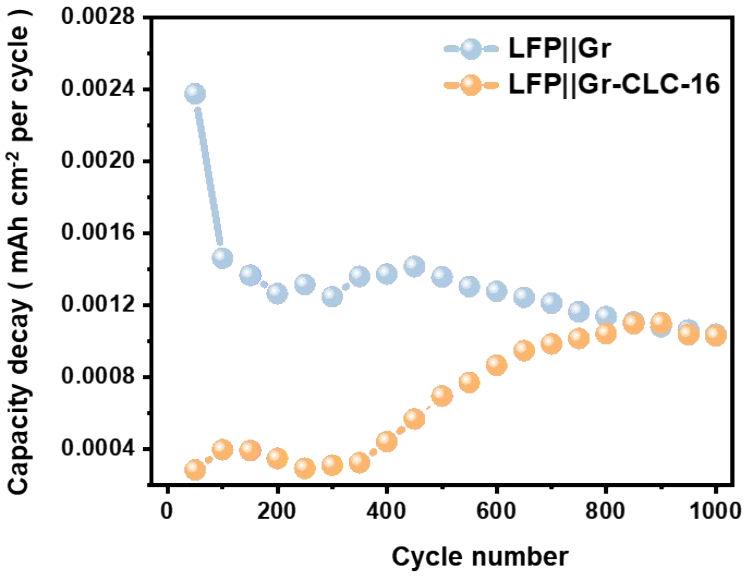

Figure S27. The capacity decay rate comparison between LFP||Gr-CLC-16 and LFP||Gr full cell.

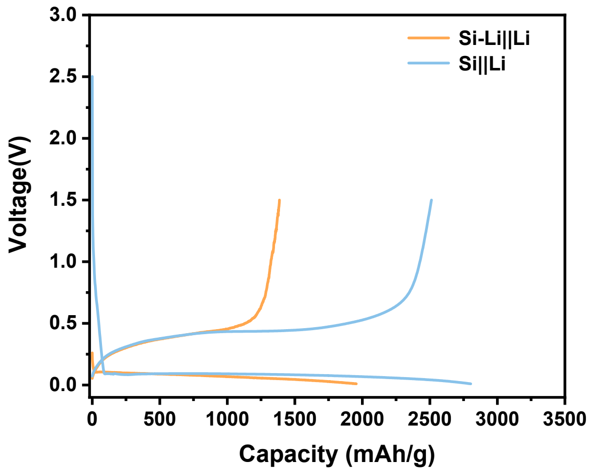

Figure S28. The discharge-charge curve of the first cycle for Si-LiAg||Li and Si||Li half cell.

Table S1. Comparison of electrochemical performances of batteries with prelithiation

Battery Type	ICE (%)	Current Density	Cycles	Capacity Retention	Area Capacity (mAh cm^{-2})	Reference
LFP‖Gr	94.9	0.2C	200	77%	0.93	[1]
LFP‖Gr	/	0.2C	60	99.3%	0.77	[2]
LFP‖Gr	95.88	0.5C	195	99.8%	0.9	[3]
LCO‖Gr	94.3%	0.2C	100	78.4%	2.16	[4]
LFP‖Gr	97%	0.56C	60	/	0.48	[5]
LFP‖Gr	98%	0.2C	60	92.1%	1.28	[6]
LFP‖Gr	98.4%	0.1C	100	94.6%	3.4	[7]
LFP‖Gr	92%	0.3C	400	96%	3.3	Our work

The calculation of Li+ releasing rate during full cell cycling.

The Li^+ releasing rate from CLC during each cycle of the full cell is calculated as follows:

$$Q_{compensated}(n) = Q_{charge}(n) * (CE_{CLC-16}(n) - CE_{Gr}(n))$$

Where n represents the nth cycle, $Q_{charge}(n)$ and $CE_{CLC-16}(n)$ represents the charge capacity and the Coulombic efficiency for LFP||Gr-CLC-16. $CE_{Gr}(n)$ corresponds to the Coulombic efficiency for LFP||Gr full cell.

The energy density comparison for LFP||Gr-CLC-16 and LFP||Gr-contact prelithiation

Due to the presence of pinholes on CLC-16, the actual area density of CLC-16 is 8.84 mg cm^{-2} (based on the average value of 10 pieces of CLC-16 disks with a diameter of 12mm), only slightly higher than that of 10 μm-thick Cu foil (8.63 mg cm^{-2}). In contrast, with contact prelithiation, the extra graphite loading to prevent lithium deposition results in a mass increase of 2.68 mg cm^{-2}, far surpassing that brought by CLC-16. The energy density was determined based on the total mass of the electrodes, electrolyte, and separator as follows:

$$Energy\ density\ (ED) = \frac{Discharge\ energy}{M_{anode} + M_{cathode} + M_{electrolyte} + M_{separator}}$$

The energy density for the initial cycle of the LFP||Gr-CLC-16 and LFP||Gr-contact prelithiation is calculated:

$$ED_{CLC-16} = \frac{0.010671\ Wh}{(0.0223 + 0.02887 + 0.01342 + 0.00177) * 10^{-3} kg} = 160.80\ Wh/kg$$

$$ED_{Contact\ prelithiation} = \frac{0.011098\ Wh}{(0.02579 + 0.02887 + 0.01342 + 0.00177) * 10^{-3} kg} = 158.88\ Wh/kg$$

Hence, although the discharge capacity of the LFP||Gr-CLC-16 is slightly lower than that of contact prelithiation, the energy density of the Gr-CLC-16 surpasses that of Gr-contact prelithiation from the initial cycling

Reference

1. S. Xu, Q. Fang, J. Wu, S. Weng, X. Li, Q. Liu, Q. Wang, X. Yu, L. Chen, Y. Li, Z. Wang and X. Wang, Small, 2024, 20, 2305639.
2. X.-Y. Yue, Y.-X. Yao, J. Zhang, S.-Y. Yang, Z. Li, C. Yan and Q. Zhang, Advanced Materials, 2022, 34, 2110337.
3. C. Yang, H. Ma, R. Yuan, K. Wang, K. Liu, Y. Long, F. Xu, L. Li, H. Zhang, Y. Zhang, X. Li and H. Wu, Nature Energy, 2023, 8, 703-713.
4. X. Zhao, R. Yi, L. Zheng, Y. Liu, Z. Li, L. Zeng, Y. Shen, W. Lu and L. Chen, Small, 2022, 18, 2106394.
5. Y. Shen, X. Shen, M. Yang, J. Qian, Y. Cao, H. Yang, Y. Luo and X. Ai, Advanced Functional Materials, 2021, 31, 2101181.
6. X.-Y. Yue, Y.-X. Yao, J. Zhang, Z. Li, S.-Y. Yang, X.-L. Li, C. Yan and Q. Zhang, Angewandte Chemie International Edition, 2022, 61, e202205697.
7. C. Wang, F. Yang, W. Wan, S. Wang, Y. Zhang, Y. Huang and J. Li, Energy & Environmental Science, 2023, 16, 4660-4669.